Part I: An X-Ray Scattering Study of Cholera Toxin Penetration and Induced Phase Transformations in Lipid Membranes

C. E. Miller,* J. Majewski,* E. B. Watkins,*§ and T. L. Kuhl†‡

*Manuel Lujan Neutron Scattering Center, Los Alamos National Laboratory, Los Alamos, New Mexico; †Department of Chemical Engineering and Material Science, University of California, Davis, California; ‡Department of Biomedical Engineering, University of California, Davis, California; and §Biophysics Graduate Group, University of California, Davis, California

ABSTRACT Cholera toxin is a highly efficient biotoxin, which is frequently used as a tool to investigate protein-membrane interactions and as a reporter for membrane rafts. Cholera toxin binds selectively to gangliosides with highest affinity to GM_1. However, the mechanism by which cholera toxin crosses the membrane remains unresolved. Using x-ray reflectivity and grazing incidence diffraction, we have been able to monitor the binding and penetration of cholera toxin into a model lipid monolayer containing the receptor GM_1 at the air-water interface. Very high toxin coverage was obtained allowing precise measurements of how toxin binding alters lipid packing. Grazing incidence x-ray diffraction revealed the coexistence of two monolayer phases after toxin binding. The first was identical to the monolayer before toxin binding. In regions where toxin was bound, a second membrane phase exhibited a decrease in order as evidenced by a larger area per molecule and tilt angle with concomitant thinning of the monolayer. These results demonstrate that cholera toxin binding induces the formation of structurally distinct, less ordered domains in gel phases. Furthermore, the largest decrease in lateral order to the monolayer occurred at low pH, supporting a low endosomal pH in the infection pathway. Surprisingly, at pH = 8 toxin penetration by the binding portion of the toxin, the B_5 pentamer, was also observed.

INTRODUCTION

Many bacterial toxins bind to and gain entrance to target cells through specific interactions with membrane components. One such example is cholera toxin ($CTAB_5$), a pathologically active agent secreted by the bacterium *Vibrio cholerae* (1). The toxin has an AB_5 arrangement of subunits. Five identical B subunits (CTB_5), each composed of 103 amino acids, form a pentameric ring with a vertical height of 32 Å and a radius of 31 Å (2,3). CTB_5 is responsible for binding the toxin to its cell-surface receptor and has highest affinity to ganglioside GM_1. The A subunit is composed of a disulfide-linked A1 and A2-subunit that is aligned through the pentameric ring (''doughnut hole'') of the B_5 subunit. After binding to intestinal cells, $CTAB_5$ travels from the plasma membrane to the endoplasmic reticulum (ER) (4). It has been proposed that proteolytic cleavage (between residues 192 and 194) and reduction of the disulfide bond (Cys-187 = Cys-199) activates the A1 peptide enabling it to cross the cell membrane (5). On the cytoplasmic side of the membrane, the A1 peptide interacts with integral membrane proteins, disrupting their normal function, resulting in a large efflux of water and ions from the cell (severe diarrhea) (6). Although much is known about the structure and catalytic activity of cholera toxin, the mechanism by which cholera toxin crosses the plasma membrane remains unresolved.

Because of its detrimental effect on health, cholera toxin has been the focus of many studies. Several different methods have shown that the B_5 portion of the toxin is responsible for binding to lipid membranes containing GM_1. Experiments involving electron microscopy, ellipsometry, and flow cytometry indicate that cholera toxin has minimal, nonspecific adsorption to lipid membranes in the absence of ganglioside lipids (7–9). Because binding is multivalent (one GM_1 per B monomer), off-rates of the toxin are slow to make the CTB_5-GM_1 complex very stable. If the concentration of GM_1 receptor is large enough, it is possible for macroscopic, two-dimensional (2D) cholera toxin crystals to be assembled with high coverage (7). See Part II in this issue for details about diffraction from the 2D cholera toxin layer. At the molecular level, atomic force microscopy studies have shown that CTB_5 binds to GM_1 rich domains of lipid bilayers and is used as a marker for lipid raft domains (10–12). Electron microscopy, impedance spectroscopy, and surface plasmon resonance have shown with reasonable confidence that the A unit faces away from the lipid layer when bound (9,13). We previously confirmed this orientation with neutron reflectivity studies (14).

In a recent study, Hammond et al. (15) have provided evidence that cholera toxin's multivalent binding to GM_1 can cause uniform liquid-ordered membranes to phase-separate into large, coexistent liquid-ordered and liquid-disordered membrane domains. It has been proposed that lateral tension gradients and hydrophobic mismatch at domain boundaries can induce membrane fusion events (16). Membrane fusion is a critical step in the endocytotic pathway and, the toxin

Submitted September 6, 2007, and accepted for publication February 12, 2008.

Address reprint requests to Tonya Kuhl, Dept. of Chemical Engineering, University of California Davis, One Shields Ave., Davis, CA 95616. Tel.: 530-754-5911; E-mail: tlkuhl@ucdavis.edu.

Editor: Thomas J. McIntosh.

0006-3495/08/07/629/12 $2.00

doi: 10.1529/biophysj.107.120725

may gain access to the cytoplasmic side of the membrane by invoking this mechanism.

Conversely, Rodighiero et al. has proposed that cholera toxin only needs to be bound to GM_1 long enough to initiate endocytosis, the cell's mode of transport to the ER (17). These studies strongly suggest that a low dissociation rate may be important for membrane penetration and support that long-term/stable formation of the multivalent CTB_5-GM_1 complex is necessary for intercellular trafficking to the ER and intoxication. It has also been proposed that once in the ER cholera toxin then uses the natural transport mechanisms of the cell, which transport misfolded proteins from the ER to the cytosol to be degraded and to traverse the membrane (18). In the last few years there has been growing consensus that cholera toxin moves from the plasma membrane to the ER, and data from four independent experimental approaches are consistent with the A1 subunit crossing the ER membrane (19).

To investigate the molecular changes that occur in membranes when toxins bind, we used a simple, model system consisting of a two-component lipid monolayer at the air-water interface, where one component was GM_1. The other component, dipalmitoyl-phosphoethanolamine (DPPE), has previously been established to mix well with GM_1 (20). Using x-ray scattering, we have investigated the interactions between these model membranes and cholera toxin as depicted in the schematic representation in Fig. 1. We have investigated the cholera-lipid system at pH = 8, which approximates the environment exterior to the cell, and at pH = 5, which represents the low endosomal pH to which the toxin would be subjected after endocytosis.

These x-ray scattering studies indicate that the B_5 pentamer could play an active role in initiating endocytosis through membrane perturbation. In addition to binding and creating a site for membrane fusion, a crucial step of endocytosis, CTB_5 must remain attached to the membrane long enough to undergo endocytosis and trafficking to the ER. After cholera toxin has been engulfed by endocytosis, endosomes are known to lower pH to aid the degradation of cellular components such as lipids and proteins. Consistent with this mechanism, our grazing incidence diffraction results show the largest perturbation to lipid order at pH = 5.

To more clearly report our findings and to accommodate the large data set, we have divided the work into two parts. Part I reports x-ray reflectivity of the cholera-membrane system and grazing incidence diffraction from the lipid monolayer. Part II addresses grazing incidence diffraction from the bound toxin layer crystallized under the lipid monolayer.

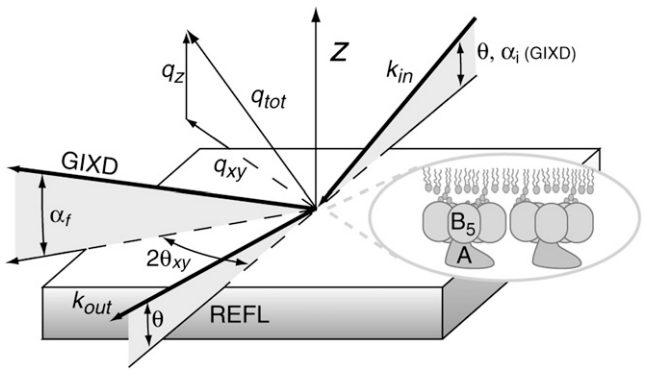

FIGURE 1 Scattering geometry for GIXD and XR. For XR, $2\theta_{xy} = 0$ and θ is changing. During GIXD, the angle of incidence, α_i, of the x-ray beam is less than the angle of total external reflection from the air-water interface. The cartoon is a schematic representation of the lipid-protein system. The lipid monolayer is composed of an 80:20 mol % mixture of DPPE:GM_1. CTB_5 and $CTAB_5$ bind to the monolayer in the approximate orientation shown.

MATERIALS AND METHODS

Materials

All lipid monolayers were composed of 80:20 mol % of DPPE:GM_1 [1, 2-dipalmitoyl-*sn*-glycero-3-phosphoethanolamine:galactosyl-*N*-acetylgalactosaminyl (*N*-acetyl-neuraminyl) galactosylglucosylceramide (GM_1 ganglioside)]. GM_1 and DPPE were obtained from Avanti Polar Lipids (Alabaster, AL) and were used without further purification. Lipids were dissolved in chloroform/methanol, 90:10, v/v (~1.2 mg/mL); mixed to obtain an 80:20 mol ratio; and deposited on an H_2O buffer subphase (pH = 5 or pH = 8). Buffer chemicals were purchased from Sigma (St. Louis, MO) and prepared using Millipore H_2O with 170 mM NaCl, 1.4 mM sodium azide, 0.3 mM EDTA, 15 mM Trizma-HCl (pH = 5)/ 15 mM Trizma-Base (pH = 8). Cholera toxin, $CTAB_5$, was purchased from BioMol Research Labs (Plymouth Meeting, PA), and CTB_5 was purchased from Sigma. Cholera toxin in powder form was dissolved in water to a concentration of 1 mg/mL. One mL of the cholera solution was then injected into the subphase (under the monolayer) to a final concentration of ~4 mg/L. The subphase was continuously circulated by a peristaltic pump at a rate of ~8 mL/min. This procedure homogenized the concentration of the toxin throughout the volume of the trough (240 mL). Cholera toxin was allowed to incubate for 1–3 h before scanning. To ''activate'' cholera toxin, we used dithiothreitol (DTT) to reduce the disulfide bond (Cys-187=Cys-199) between the the A1 and A2 subunit. DTT (Cleland's reagent) is frequently used to reduce the disulfide bonds of proteins though it is unable to reduce buried (solvent-inaccessible) disulfide bonds. Dithiothreitol (DTT) was purchased from Sigma and injected into the subphase to a final concentration of 4.6 mg/mL and was circulated for 1–3 h before scanning. Unless otherwise noted, the monolayer's molar composition, surface pressure of 20 mN/m, and temperature of 23°C were held constant throughout each experiment. These conditions approximate the surface pressure of a physiological cellular membrane. Unless otherwise noted, the same monolayer was used without respreading for a sequence of experiments involving the bare monolayer, toxin injection ($CTAB_5$ or CTB_5), and addition of DTT.

X-ray reflectivity

All synchrotron x-ray measurements were carried out using the liquid surface diffractometer at the BW1 (undulator) beam line at Hamburger Synchrotronstrahlungslabor (HASYLAB) at Deutsche Elektronen-Synchrotron (DESY) (Hamburg, Germany). A temperature controlled Langmuir trough equipped with a Wilhelmy balance for surface pressure measurements and a motorized barrier for surface area variation was mounted on the diffractometer. The trough was enclosed in a sealed, helium-filled canister where the oxygen level was constantly monitored. The synchrotron x-ray beam was monochromated to a wavelength of $\lambda \approx 1.304$ Å. The theory of x-ray reflectivity (XR) and grazing incidence x-ray diffraction (GIXD) has been presented in detail elsewhere (21–24) and only a brief discussion will be given here.

Reflectivity, R, is defined as the ratio of the intensity of x-rays specularly reflected from a surface relative to that of the incident x-ray beam. When

measured as a function of wave-vector transfer ($q_z = |\boldsymbol{k}_{out}-\boldsymbol{k}_{in}| = 4\pi\sin\theta/\lambda$, where θ is the grazing angle and λ is the wavelength of the x-ray beam, Fig. 1), the reflectivity curve contains information on the sample-normal profile of the in-plane average of the electron density. Typical scanning times for this q_z range were 30 min. The absolute reflectivity was derived by subtracting background followed by normalization to the incident beam flux. The data were reduced and plotted as R/R_F versus the perpendicular scattering vector, q_z (the division by Fresnel reflectivity, R_F, increases the visibility of the reflectivity profile by removing a sharp q_z^{-4} decrease of the reflectivity due to Fresnel's law). The error bars on the data represent the statistical errors in the measurements (standard deviation, σR). Analysis of the measured reflectivity curves was performed using a model-free approach (25). In this method, the electron density profile was parameterized using cubic B-splines. The coefficients in the series were determined by constrained nonlinear least-squares methods, in which the smoothest solution with the lowest χ^2 was chosen. Confidence in these models was supported by the fact that the family of models deviating by a maximum of 5% of χ^2 showed no significant changes to the electron density profile. In this manner, detailed information on the electron density distribution in the direction normal to the interface was determined. In all cases lipid phase domains were smaller than the coherency of the x-ray beam (few micrometers) (20).

Grazing incident x-ray diffraction

For the GIXD experiments, the x-ray beam was adjusted to strike the surface at an incident angle of $\alpha_i = 0.11°$ (Fig. 1), which corresponds to a vertical momentum transfer vector $q_z = 0.85\, q_c$, where $q_c = 0.02176$ Å^{-1} is the critical scattering vector for total external reflection from the liquid subphase. At this angle the incident wave is totally reflected, whereas the refracted wave is an evanescent wave traveling along the liquid surface. Such a configuration maximizes surface sensitivity. The dimension of the x-ray beam footprint on the liquid surface was ~2 mm × 50 mm. For in-plane diffraction measurements, a Soller collimator, consisting of closely spaced vertical plates, was placed before a vertical one-dimensional position sensitive detector with vertical acceptance $0 < q_z < 1.2$ Å^{-1} yielding a lateral resolution of $\Delta q_{xy} = 0.0084$ Å^{-1}.

From three-dimensional (3D) crystals, strong diffraction from a set of crystal planes with interplanar spacing d occurs only when the Bragg law ($n\lambda = 2d\sin\theta$) is obeyed. More precisely, diffraction occurs only when the scattering vector, q, coincides with points of the reciprocal 3D lattice with integer Miller indices (h, k, l), giving rise to Bragg spots. In our 2D systems, the monolayers are a mosaic of 2D crystals with random orientation about the direction normal to the subphase, and can therefore be described as 2D powders. Because of the lack of restriction on the scattering vector component q_z along the direction normal to the 2D crystal, Bragg scattering extends as continuous Bragg rods in reciprocal space (21).

The scattered intensity was measured by scanning over a range of horizontal scattering vectors,

$$\begin{aligned} q_{xy} &\equiv \left(q_x^2 + q_y^2\right)^{\frac{1}{2}} \\ &= \frac{2\pi}{\lambda}[\cos^2(\alpha_i) + \cos^2(\alpha_f) - 2\cos(\alpha_i)\cos(\alpha_f)\cos2\theta_{xy})]^{\frac{1}{2}} \\ &\cong \frac{2\pi}{\lambda}[1 + \cos^2(\alpha_f) - 2\cos(\alpha_f)\cos2\theta_{xy})]^{\frac{1}{2}}, \end{aligned}$$

where $2\theta_{xy}$ is the angle between the incident and diffracted beam projected onto the horizontal plane, q_{xy} is the combination of horizontal components q_x and q_y, and α_i and α_f are the incident and the scattered angles, respectively (21,22). Bragg peaks are the intensity resolved in the q_{xy}–direction and integrated along the z-direction. Conversely, the Bragg rod profiles are the intensity resolved in the q_z-direction (i.e., along $q_z = \frac{2\pi}{\lambda}(\sin\alpha_i + \sin\alpha_f) \approx \frac{2\pi}{\lambda}\sin\alpha_f$) and integrated over the q_{xy} range of the Bragg peak. The positions of the maxima of the Bragg peaks, q_{xy}^{max}, allow the determination of the repeat distances $d = 2\pi/q_{xy}$ of the 2D lattice. From the widths of the peaks, corrected for the instrument resolution, it is possible to determine the 2D crystalline in-plane coherence length, L_{xy} (the average distance in the direction of the reciprocal lattice vector q_{xy} over which there is near-perfect crystallinity). The intensity distribution along the Bragg rod was analyzed to determine the direction and magnitude of the molecular tilt, the coherently scattering length of the molecule, Lc, and the magnitude of molecular motion or surface roughness, σ, of the crystallite (DW factor).

Beam damage

X-rays with a wavelength of 1.304 Å (9.5 keV) can cause significant beam damage to the monolayer/toxin sample. Overexposure can ''burn'' the sample, which causes a change in the real space structure over time. For all reported measurements, the sample was translated perpendicular to the beam during scans, and every area was scanned only once to mitigate x-ray damage to the film. In addition to sample translation, repeat measurements were conducted a minimum of three times to detect any beam damage artifacts. Repeat scans over fresh regions were identical.

RESULTS AND DISCUSSION

Pressure–area isotherms

Pressure–area isotherms for GM_1, DPPE, and their mixtures are shown in previous studies (20). For the 100% GM_1 isotherm, the large size of the GM_1 headgroup caused a nonzero surface pressure even at areas per molecule >100 Å^2. This behavior is typical for a fluid phase monolayer with a large bulky headgroup (27). The pure DPPE monolayer had a much sharper pressure increase distinctive of a solid-phase monolayer. All DPPE:GM_1 lipid mixtures with 20% or less GM_1 content could be almost superimposed on the isotherm of pure DPPE. This indicated that GM_1 molecules, up to a mole fraction of 20%, are incorporated into the DPPE matrix and do not significantly disturb the packing of the DPPE molecules. This minimal perturbation can also be verified by previous work on the packing of ganglioside-phospholipid monolayers using GIXD (20). No indication of domain formation, phase separation, or nonhomogeneous structuring within the mixed monolayer at the air–water interface at 20 mN/m was observed using fluorescence, Brewster angle microscopy, or x-ray scattering methods (20).

Area expansion analysis

At a constant surface pressure of 20 mN/m, cholera toxin binding resulted in an increase in the area of the monolayer film. The relative increase in the area per lipid molecule of toxin bound at pH = 5 is shown in Fig. 2. Both CTB_5 and $CTAB_5$ were injected at $t = 0$ s, yielding similar increases in area on toxin binding. This finding demonstrates that the presence of the A subunit had little effect on the area increase before addition of DTT. The increase in area per molecule is a result of either packing inefficiencies of the lipids caused by the cholera binding, toxin insertion into the lipid monolayer, or a combination of the two. Monte Carlo simulations have previously shown that the observed area expansion upon toxin binding is consistent with packing inefficiencies caused by constraining GM_1 lipids at cholera's five binding sites (14,28).

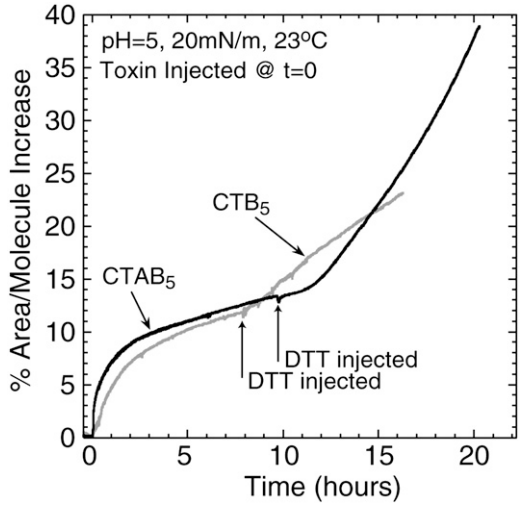

FIGURE 2 A typical area expansion of a 80:20 mol % mixture of DPPE:GM_1 monolayer at a constant pressure of 20 mN/m after injection of $CTAB_5$ and CTB_5 into the subphase at $t = 0$ s. The area expansion was similar for both toxins. After DTT was injected into the subphase and disulfide bond reduction was initiated, the rate of expansion was greatly increased for $CTAB_5$. Cholera toxin and DTT were allowed to incubate for 1–3 h before x-ray scattering experiments. Percent area/molecule increase = [(area/molecule) − (initial area/molecule)] / (initial area/molecule) × 100%.

In earlier neutron reflectivity studies, we scanned an 80:20 DPPE:GM_1 monolayer with bound $CTAB_5$ consecutively over a 16 h time period to monitor $CTAB_5$ binding as a function of time (14). After 3 h of incubation there were no significant changes in the film structure as seen by neutron reflectivity. Similarly, ellipsometry studies demonstrate that CTB_5 adsorption starts immediately after injection and is complete ~1 h after incubation (7). Our findings from trough expansion are more sensitive, showing ~80% of the expansion takes place in the first 3 h followed by a slow area increase over the next 7 h. Cholera toxin was allowed to incubate for 1–3 h before starting x-ray scattering experiments.

When DTT was injected into the subphase and enzymatic cleavage (in the case of $CTAB_5$) was initiated, it dramatically amplified the rate of area increase of the monolayer for $CTAB_5$ (Fig. 2). Surprisingly, a noticeable increase in area was also observed after injection of DTT into the subphase containing CTB_5. When DTT was added to the subphase in the absence of toxin, no area expansion was observed (< 1%).

Reflectivity analysis (pH = 8)

Toxin binding, orientation, and its effect on the lipid monolayer

Reflectivity measurements of the lipid-toxin system at the air-water interface enabled the average electron density profile normal to the interface to be determined. The experimentally measured Fresnel-divided reflectivity profiles at pH = 8 for 1), the mixed DPPE:GM_1 monolayer; 2), the monolayer with CTB_5; and 3), the monolayer with CTB_5 + DTT on an H_2O/buffer subphase are shown in Fig. 3 *a*. Fig. 3 *c* shows the experimentally measured reflectivity profiles for 1), the mixed DPPE:GM1 monolayer; 2), the monolayer with $CTAB_5$; and 3), the monolayer with $CTAB_5$ + DTT on an H_2O/buffer subphase. A few qualitative observations can be made directly from the reflectivity profiles. When either CTB_5 or $CTAB_5$ was present in the subphase, there was a shift in the first interference maximum from $q_z \approx 0.08$ Å^{-1} to smaller q_z values. This is indicative of an increased thickness of the system as a result of toxin binding and formation of a toxin layer under the lipid monolayer. Also, for both CTB_5 and $CTAB_5$ there was a significant difference in the reflectivity profile before and after injection of DTT.

More quantitative details were obtained using cubic B-spline fits to invert the reflectivity profile into real space structures. The corresponding electron density profiles, $\rho(z)$, obtained from the cubic B-spline fits (solid and dashed curves) are shown in Fig. 3 *b* and *d*. The presence of both CTB_5 and $CTAB_5$ can clearly be seen by a large electron density increase extending into the subphase from the headgroup region. Consistent with the known crystal structure of CTB_5 (3), the B_5 pentamer extends ~40 Å from the monolayer (depth 35Å–75Å). With $CTAB_5$ the curve is consistent with the A subunit facing away from the monolayer into the subphase. The total thickness of ~70 Å (depth 35Å–105Å) is again consistent with the crystal structure for $CTAB_5$ (2). This orientation and binding behavior match our previous neutron reflectivity studies (14). Importantly, the much higher resolution provided by x-ray reflectivity studies enabled the observation of changes in electron density of the lipid tail region and assessment of toxin penetration into the lipid monolayer.

Lipid monolayer region before and after injection of DTT

Fig. 4 shows a close-up of the lipid monolayer region from Fig. 3 *b* and *d*. Before injection of DTT, the electron density profile of the tail region conserved the same general shape as the monolayer before toxin was present. After injection of DTT (CTB_5 + DTT and $CTAB_5$ + DTT) there was a significant increase in electron density of the lipid tails and a significant decrease in electron density of the lipid headgroup region (Fig. 4). The decrease in headgroup density is consistent with the area increase observed on the trough, and a similar decrease in density of the tails should occur (Fig. 2). Hence, the increase in electron density in the tail region establishes penetration of toxin into the lipid monolayer. Unexpectedly, the density increase in the tail region for CTB_5 + DTT was similar to $CTAB_5$ + DTT. Previously, the B_5 pentamer portion of the cholera toxin molecule has been associated primarily with receptor binding. However, our studies clearly demonstrate that the B_5 pentamer can penetrate into the lipid region. In contrast, no penetration was observed at pH = 5, which suggests that DTT may have a

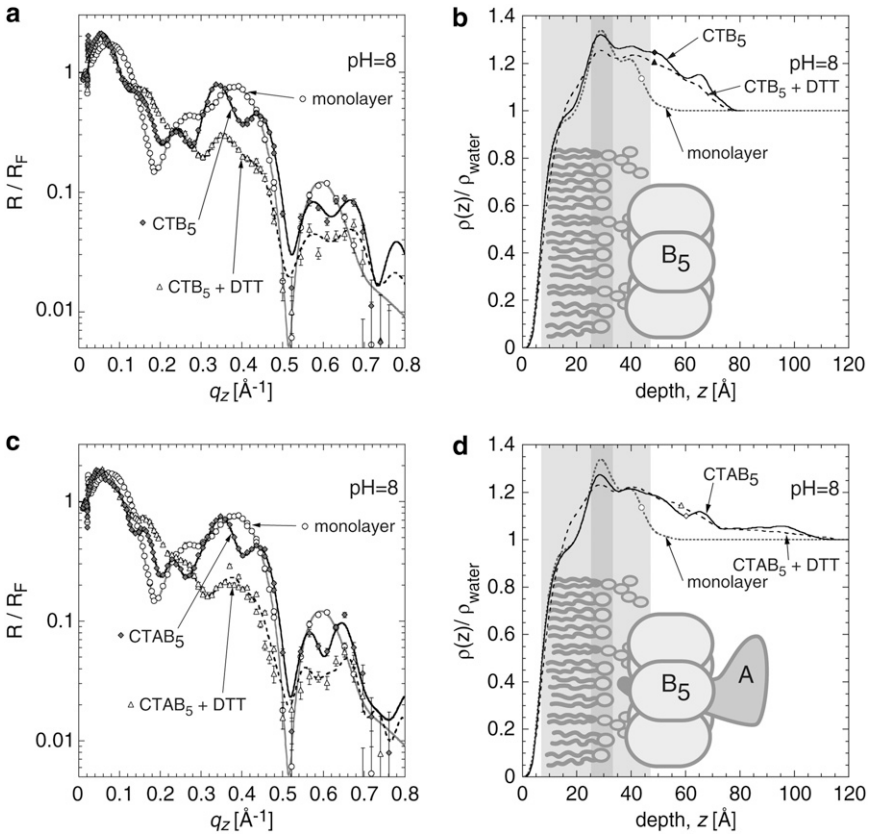

FIGURE 3 X-ray reflectivity results at pH = 8. For clarity, the experiment set is separated into two parts. (*a* and *b*) A DPPE:GM_1 monolayer with bound CTB_5 (before and after injection of DTT). (*c* and *d*) A DPPE:GM_1 monolayer with bound $CTAB_5$ (before and after injection of DTT). (*a* and *c*) The measured reflectivity plotted as $R/R_{Fresnel}$ vs. q_z. Error bars for the reflectivity data represent statistical errors in these measurements. Measured data are represented as symbols, and lines (*solid* and *dashed*) represent fits corresponding to the electron density profiles shown in *b* and *d*. The electron densities $\rho(z)$ are normalized to the electron density of water, ρ_{water} 0.334 $e^-/Å^{-3}$. In the electron density profiles the binding of both CTB_5 and $CTAB_5$ can clearly be seen by a large electron density increase extending into the subphase from the GM_1 headgroup region. Binding of toxin results in a decrease in electron density in the headgroup region and a small increase in density in the lipid tail region. After injection of DTT, there was a substantial density increase in the lipid tail region suggesting that both CTB_5 and $CTAB_5$ are entering the lipid region (Fig. 4). Surprisingly, CTB_5 and $CTAB_5$ had similar effects on the lipid monolayer at pH = 8. These results are distinctly different from results at pH = 5 (discussed later).

larger effect on the B_5 pentamer conformation at the higher pH. In control measurements, no density change was observed in the tail region for monolayers after addition of DTT with no toxin present.

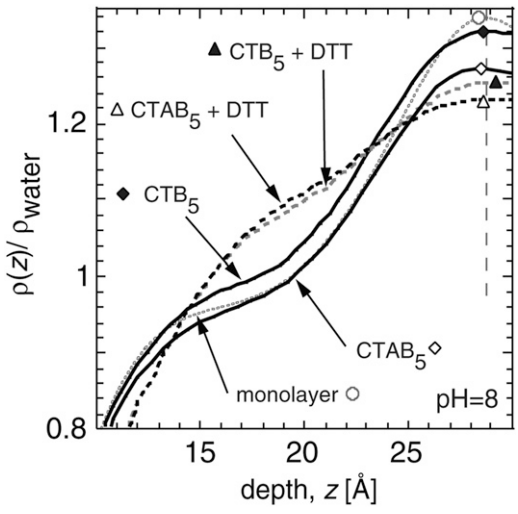

FIGURE 4 Close-up of the electron density profile of the lipid monolayer region from Fig. 3, *b* and *d*. All curves are referenced to the headgroup peak density (*dotted vertical line*). Before injection of DTT, the electron density profile of the tail region had the same characteristics as the monolayer before toxin was present. After injection of DTT, both CTB_5 and $CTAB_5$ caused a significant increase in density of the tail region suggesting that toxin entered the lipid region of the monolayer.

Reflectivity analysis (pH = 5)

Low pH prevented CTB_5 + DTT from perturbing the monolayer

The experimentally measured reflectivity profiles at pH = 5 for 1), the mixed DPPE:GM1 monolayer; 2), the monolayer with CTB5; and 3), the monolayer with CTB_5 + DTT on an H_2O/buffer subphase are shown in Fig. 5 *a*. Fig. 5 *c* shows the experimentally measured reflectivity profiles for 1), the mixed DPPE:GM1 monolayer; 2), the monolayer with CTAB5; and 3), the monolayer with CTAB5 + DTT on an H2O/buffer subphase. Electron density profiles obtained from cubic B-spline fits to the reflectivity data at pH = 5 for CTB_5 and $CTAB_5$ are shown in Fig. 5 *b* and Fig. 5 *d* respectively. The monolayer regions for bound $CTAB_5$ and $CTAB_5$ + DTT look very similar to the lipid monolayer regions at pH = 8 where there is minimal perturbation to the monolayer before injection of DTT and a large increase in lipid tail density after injection of DTT. Conversely, with CTB_5 there was almost no change in the reflectivity (Fig. 5 *a*) or real space structure (Fig. 5 *b*) after adding DTT at pH = 5. These results were consistent between several independent experiments.

Cholera toxin coverage under the lipid monolayer

The electron density profiles obtained from reflectivity analysis were used to quantitatively determine the amount of

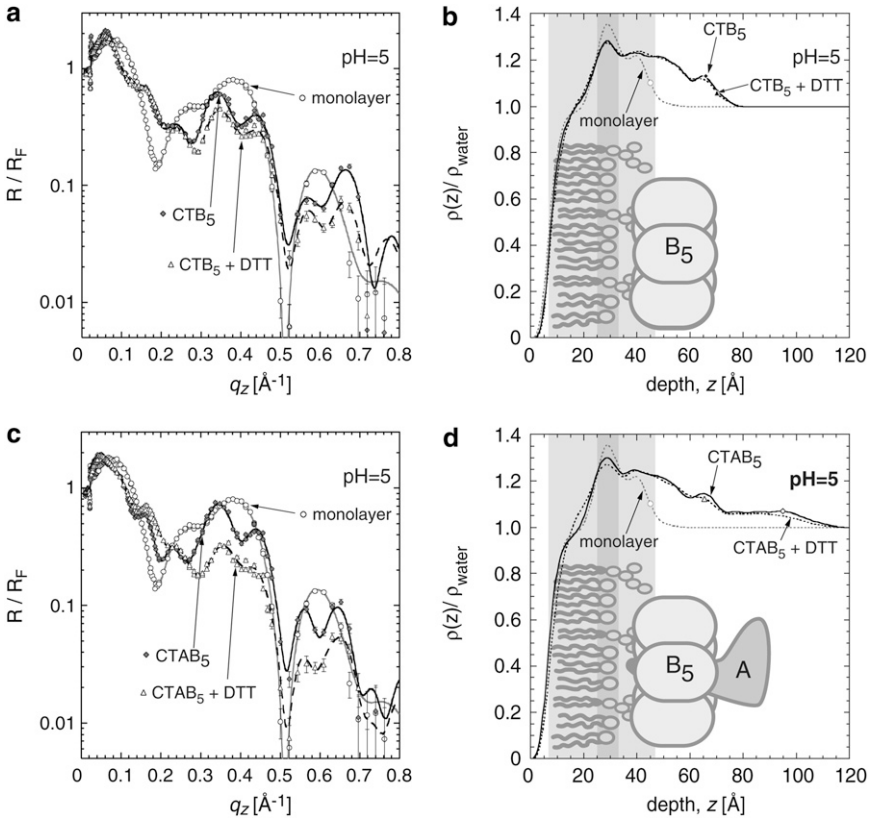

FIGURE 5 XR results at pH = 5. (*a* and *b*) A DPPE:GM_1 monolayer with bound CTB_5 (before and after injection of DTT). (*c* and *d*) A DPPE:GM_1 monolayer with bound $CTAB_5$ (before and after injection of DTT). (*a* and *c*) The measured reflectivity plotted as $R/R_{Fresnel}$ vs. q_z. Error bars for the reflectivity data represent statistical errors in these measurements. Measured data are represented as symbols, and lines (*solid* and *dashed*) represent fits corresponding to the electron density profiles shown in *b* and *d*. There is one major difference observed when compared to XR results at pH = 8. CTB_5 + DTT did not significantly perturb the electron density of the lipid monolayer region. This similarity can be seen both in the measured reflectivity profiles (*a*) and the electron density profiles (*b*). As in the case of pH = 8, $CTAB_5$ + DTT caused a large electron density increase in the lipid tail region.

toxin bound to the monolayer. Two examples for CTB_5 and $CTAB_5$ at pH = 5 are shown in Fig. 6. The toxin coverage was quite high, typically ~50%. The % coverage, X, was calculated using the following equation:

$$\rho(z)^{\#}_{\text{measured}} = [1 - X][\rho_{\text{water}}] + [X][(0.936^{\&})\rho^{\S}_{\text{CTB5}} + (0.064^{\&})\rho_{\text{water}}],$$

where:

$\rho(z)$ = measured electron density.

X = % coverage of CTB_5.

$\rho_{\text{water}} = 0.334\ e^{-}/\text{Å}^{-3}$.

[#]Measured electron density values $\rho(z)$ were taken from both CTB_5 profiles in Fig. 6 *a* at a depth $z \approx 50$ Å. The measured maximal and minimal electron densities of $0.404\ e^{-}/\text{Å}^{-3}$ and $0.422\ e^{-}/\text{Å}^{-3}$ lead to 49% and 62% coverage, respectively.

The volume of CTB_5 was approximated by a regular pentagon with sides of length 36 Å and a height of 32 Å: $5/4 \times 36 \times 36 / \tan(36) \times 32 = 71{,}351\ \text{Å}^3$. The central pore volume was approximated by a cylinder with a diameter of 13.5 Å and a height of 32 Å: $\pi/4 \times 13.5 \times 13.5 \times 32 = 4580\ \text{Å}^3$. Hence the volume of CTB_5, less the pore, is $71{,}351 - 4580 = 66{,}771\ \text{Å}^3$. These distances were obtained from the 3D crystal structure (3).

[&]Volume fractions obtained from the ratio of CTB_5 volume ($66{,}771\ \text{Å}^3$) and the central pore volume ($4580\ \text{Å}^3$) to the total volume: 0.064 = 4580/71,351, 0.936 = 66,771/71,351.

[§]$\rho_{\text{CTB5}} = 0.486\ e^{-}/\text{Å}^{-3}$. The theoretical electron density of CTB_5 was obtained by dividing the total number of electrons in CTB_5 (32,470) by its volume ($66{,}771\ \text{Å}^3$).

Although toxin coverage of the lipid monolayer ranged from 49% to 62%, these variations led to negligible differences in the electron density of the lipid tail region. As a result, the differences that were observed between pH values (Figs. 3 and 5) cannot be attributed to variable amounts of toxin coverage. Likewise, in control experiments we explored the effects of DTT without toxin on the monolayer. When no toxin was present at pH = 5 and pH = 8, DTT had no effect on area per molecule, electron density, or in-plane diffraction as measured by x-ray reflectivity and GIXD (data not shown).

GIXD analysis (pH = 8)

GIXD measurements provide in-plane structural information of the ordered, diffracting portion of the monolayer. In general, the diffraction from the lipid-toxin system was observed only in two regions. The first low q_{xy} region from 0.08 Å^{-1} to 0.35 Å^{-1} corresponds to real-space d-spacings of ~80–18 Å and diffraction from the 2D ordering of the cholera toxin layer. The second q_{xy} region from ~1.3 to ~1.6 Å^{-1} corresponds to

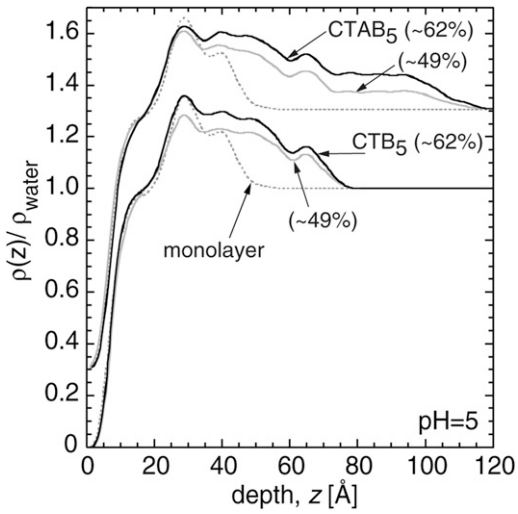

FIGURE 6 The electron density profiles illustrate the variance in the amount of toxin coverage between samples. Shown are two data sets for CTB_5 and two for $CTAB_5$, all at pH = 5. Both $CTAB_5$ profiles have been shifted up 0.3 for clarity. The calculated coverage ranged from 49% to 62%, consistent with the area expansion measured on the trough. There are small differences in the electron density of the monolayer region when different amounts of toxin are bound, but these are not sufficient to account for the variation in monolayer perturbation and toxin penetration at different pH (Fig. 4).

d-spacings of ~4.4–4.2 Å and diffraction from the DPPE:GM_1 alkyl tails. No diffraction from the lipid headgroups was detected. Here we discuss diffraction from the lipid tails. In Part II, diffraction from the toxin layer is reported (29).

Diffraction from the lipid monolayer

The diffraction pattern obtained for a pure DPPE:GM_1 monolayer at pH = 8 and 20 mN/m is shown in Fig. 7 *a* and summarized in Table 1 (phase 1). Three Bragg peaks were observed at $q_{xy} = 1.42$ Å^{-1}, $q_{xy} = 1.45$ Å^{-1} and $q_{xy} = 1.49$ Å^{-1}. The presence of three Bragg peaks is indicative of an oblique 2D cell. The integrated intensities of the Bragg peaks (-0.05 Å$^{-1} \le q_z \le 0.9$ Å^{-1}) were approximately the same in agreement with the multiplicity rule. The observed *d*-spacings, $d_{10} = 4.41$ Å ($dxy = 2\pi/qxy$), $d_{01} = 4.33$ Å, and $d_{1\text{-}1} = 4.22$ Å, give rise to a primitive 2D unit cell with dimensions of $|\boldsymbol{a}| = 4.99$ Å, $|\boldsymbol{b}| = 4.89$ Å, and $\gamma = 117.8$ degrees and an area per two alkyl chains of 43.2 Å^2.

Assuming the monolayer consists of perfect 2D crystallites of finite average dimension L_{xy} (the lateral coherence length) in the crystallographic direction $\{h, k\}$ with no preferred azimuthal orientation, the Scherrer formula (30), can be used to calculate the coherence length in the three crystallographic directions from

$$L_{xy} \approx 0.9[2\pi/FWHM_{intrinsic}(q_{xy})]\{h, k\}.$$

As the corresponding full width at half maximum (FWHM) of the three peaks exceeds the instrumental resolution of $FWHM_{resol}(q_{xy}) = 0.0084$ Å^{-1}. The intrinsic FWHM can be obtained using the equation:

$$FWHM_{intrinsic}(q_{xy}) = \left[FWHM_{meas}(q_{xy})^2 - FWHM_{resol}(q_{xy})^2\right]^{1/2}.$$

From this straightforward analysis, the lateral coherence lengths for the three peaks were $L_{10} = 196$ Å, $L_{01} = 196$ Å, and $L_{1\text{-}1} = 660$ Å. A distance of 660 Å is ~140 alkyl chains or a crystalline domain 70 lipids across.

The combined Bragg rod profile of the {0,1}, {1,0}, and {1,−1} reflections, shown in Fig. 7 *b*, was produced by integrating through the 1.38 Å$^{-1} \le q_{xy} \le 1.55$ Å^{-1} region of the three peaks. Analysis of the Bragg rod profile was done by approximating the lipid alkyl tails as tilted cylinders with constant electron density and length L_c (21). See Table 1 for the numerical results of this analysis. To check the validity of our fitting procedure, we separated each Bragg peak and fit each corresponding Bragg rod separately (shown in Fig. 7 *b*). The result was comparable to that obtained by fitting the combined Bragg rod profile of the {0,1}, {1,0}, and {1,−1} reflections. Diffraction from a control DPPE:GM_1 monolayer at pH = 8, in the absence of toxin, showed that the molecules tilt 22 ± 2.0° from the surface normal with an azimuthal angle of 13.7 ± 2.0° from the nearest neighbor defined by the vector **a** + **b**. The length of the cylinder with constant elec-

TABLE 1 In-plane structural parameters obtained from GIXD analysis

20 mN/m, 23°C	Primitive unit cell *a*, *b*, γ (Å, Å, degrees)			Area per molecule (Å^2)	Cylinder radius (Å)	Coherence length, L_c (Å)	Tilt angle, *t* (°)	Tilt direction from NN, nonsymmetry (°)	σ (Å)
Phase 1 pH = 8	4.89 ± 0.01	5.00 ± 0.01	117.7 ± 0.4	43.3 ± 0.4	1.5*	20.1 ± 0.5	22.3 ± 1.0	13.7 ± 1.0	1.0 ± 0.5
Phase 2 pH = 8	5.77 ± 0.01	5.77 ± 0.01	130.4 ± 0.4	50.7 ± 0.5	1.5*	18.6 ± 0.5	36.2 ± 2.0	30.0 ± 0.8	2.6 ± 0.1
Phase 1 pH = 5	4.89 ± 0.01	4.99 ± 0.01	117.9 ± 0.2	43.1 ± 0.2	1.5*	19.9 ± 0.5	22.9 ± 1.0	13.9 ± 1.0	2.1 ± 0.1
Phase 2 pH = 5	5.77 ± 0.01	5.77 ± 0.01	130.4 ± 0.4	50.7 ± 0.5	1.5*	18.6 ± 1.5	37.1 ± 3.0	28.4 ± 3.0	2.6 ± 0.3

Phase 1 represents the structure of the bare monolayer (Fig. 8 *a*) or, in other words, where no toxin was bound. Phase 2 represents the highly tilted toxin-affected phase (Fig. 8 *b*) or where toxin was bound. L_c is the length of the coherently scattering part of the alkyl tail measured along its backbone. σ is the vertical DW factor or root mean-square molecular displacement normal to the surface. Nearest neighbor (NN) is along **a** + **b,** where **a** and **b** are the 2D unit cell vectors.

*Fixed for modeling.

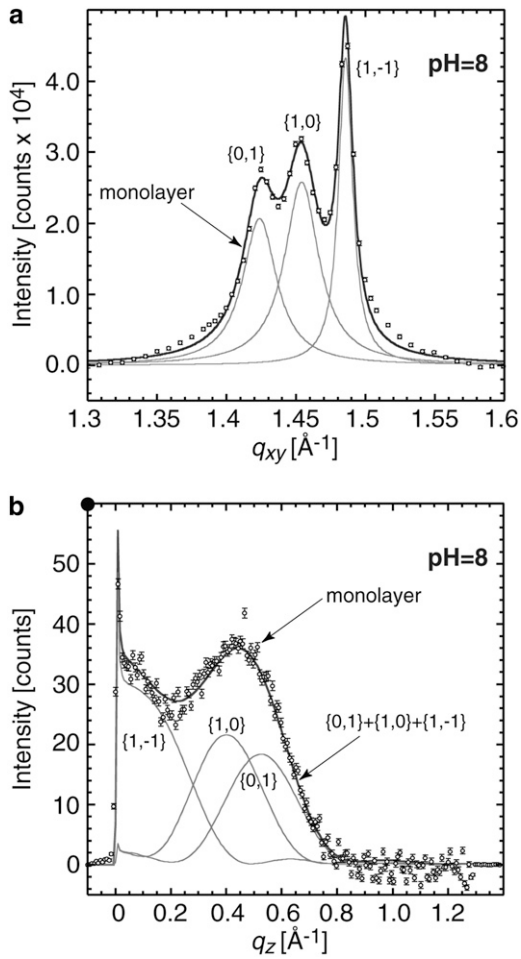

FIGURE 7 GIXD from the ordered alkyl tail regions at pH = 8 of a DPPE:GM_1 monolayer. Bragg peaks are shown in *a* and the total Bragg rod (sum of the three individual Bragg rods) is shown in *b*. The individual Bragg rod reflections are shown in gray. The three GIXD Bragg peaks observed indicate packing of the lipid tails in an oblique 2D unit cell. The Miller indices $\{h, k\}$ are indicated for each peak. Bragg peaks in *a* were obtained by integrating over the (-0.05 Å$^{-1} \leq q_z \leq 0.9$ Å^{-1}) region and each peak was fitted using a Voight function (*gray solid lines*). By integrating over the (1.38 Å$^{-1} \leq q_{xy} \leq 1.55$ Å^{-1}) region, the Bragg rod (*b*) was fitted (*solid line*) by approximating the coherently scattering part of the alkyl tail by a cylinder of constant electron density. The sharp peak at $q_z = 0.01$Å^{-1} is the so-called Yoneda–Vineyard peak (38), which arises from the interference between x-rays diffracted up into the monolayer and x-rays diffracted down and then reflected up by the interface. The molecular packing parameters used in the fitting are listed in Table 1.

tron density used to model the intensity distribution along the Bragg rods, L_c, was 20.0 ± 1.0 Å. This length is consistent with a calculated length of 20.2 Å for a 16-carbon lipid tail.

Interaction with the toxin yielded a new monolayer phase

In an extreme case, interactions with $CTAB_5$ led to striking changes in the diffraction pattern of the lipids and a new phase as illustrated in Fig. 8. In this case, the oblique unit cell of the pure monolayer (Fig. 8 *a*) was almost entirely converted to a new, second phase in which the diffraction pattern was a single peak at $q_{xy} \approx 1.43$ Å^{-1} with its maximum intensity located off the horizon at $q_z \approx 0.52$ Å^{-1} (Fig. 8 *b*) with only traces of the initial monolayer phase 1 remaining at $q_{xy} \approx 1.48$ Å^{-1}. The Bragg peaks of this new ''toxin-affected'' phase 2 are shown in Fig. 8 *c*, and Bragg rods are shown in Fig. 8 *d*. The intensity distribution along the Bragg rod is consistent with a molecular tilt of 37.2° away from the surface normal. Since there was no scattered intensity observed at small q_z values (close to the horizon), the azimuthal direction of the tilt of the alkyl tails of the monolayer has to be in the direction of the second nearest neighbor: ~30° from the nearest neighbor defined by the vector **a** + **b**. If we assume that the lipid tails pack as close packed hard cylinders, then the tilt and tilt direction are linked to the in-plane lattice parameters (31). As the data show only one diffraction peak (rod) at $q_{xy} = 1.43$ Å^{-1} and $q_z = 0.52$ Å^{-1}, we can assume that this rod is a superposition of two rods {0,1} and {1,0}, respectively. However the Peterson rule (23,32) requires one more rod, in our case the {1,−1}, at (q_{xy},q_z) = ($q_{(1,-1)}$, 1.04 Å^{-1}). The q_{xy} position of this peak can be calculated based on Eq. 19 in Kjaer et al. (31), which gives the value of $q_{(1,-1)}$= 1.20 Å^{-1}. The obtained q_{xy} values yield an increased area per lipid molecule of 50.7 Å^2 compared to 43.2 Å^2 for the pure monolayer (phase 1). However, no peak was visible at q_{xy} = 1.20 Å^{-1} (data not shown). An explanation for this is an increase to the vertical Debye-Waller (DW) factor of 2.6 Å, which dampens or suppresses the {1,−1} reflection at $q_{xy} \approx$ 1.2 Å^{-1} and $q_z \approx 1.04$ Å^{-1}. A vertical DW factor of 2.6 Å is consistent with the significant perturbation of monolayer structure as evidenced by changes in the reflectivity, area expansion, and in-plane diffraction, when cholera toxin binds. Phase 2 was most evident in these experiments; however, this new phase was present at a significant percentage in all cholera toxin binding studies as further detailed below.

Alternatively, to explain the missing diffraction peak at (q_{xy}, q_z) = (1.20 Å^{-1}, 1.05 Å^{-1}) one might hypothesize the lipid tails in phase 2 have only one-dimensional order. Such a configuration would also yield a single diffraction peak. However, one-dimensional disorder has never been previously observed for lipid tails. Moreover, the ordered direction would likely be orthogonal to the tilt direction so that the surviving peak would be at the horizon, not off-horizon as observed.

A third possibility occurs if all three diffraction peaks are superimposed at $q_{xy} = 1.43$ Å^{-1} (still obeying the Peterson rule), but cannot be resolved due to instrumental resolution. Such a lipid tail configuration would lead to the area per lipid molecule of 44.4 Å^2. However, we were unable to fit three separate Bragg rods from the rod presented in Fig. 8 *d* with the constraints imposed by the Peterson rule and the multiplicity rule, which require the integrated intensities of the peaks to be approximately equal. Therefore, the most reasonable lipid tail arrangement in phase 2 is that of close-packed cylinders in a distorted hexagonal cell with the unit vector $\mathbf{a}_h = 5.77$, $\gamma = 130.4°$, and area per molecule = 50.7 Å^2

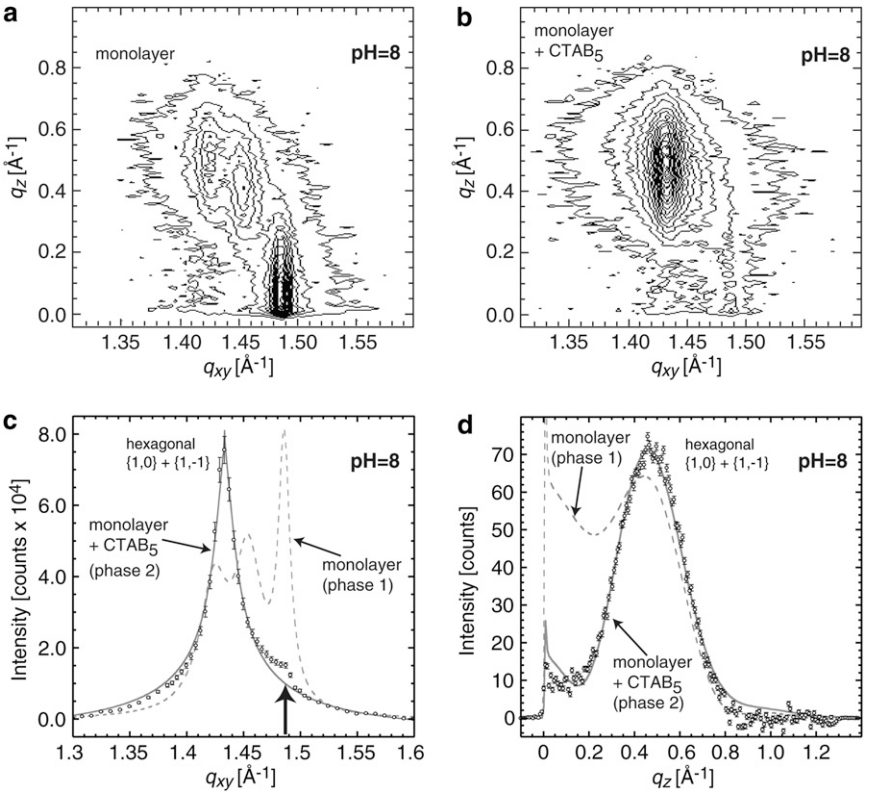

FIGURE 8 (*a*) Reciprocal space contour plot, $I(q_{xy}, q_z)$, of a pure monolayer at pH = 8 (phase 1). The integrated Bragg peaks and Bragg rods for the pure monolayer phase are shown in Fig. 7. (*b*) Reciprocal space contour plot, $I(q_{xy}, q_z)$, after injection of $CTAB_5$ at pH = 8. The dramatic change in intensity distribution between *a* and *b* signifies a different packing distribution of the lipid tails into a new monolayer phase (phase 2). This is an extreme case of cholera toxin's perturbation to the lipid monolayer and the lack of phase 1 enabled the unit cell for phase 2 to be extracted. (*c*) Bragg peaks corresponding to *b*. Bragg peaks in *c* were obtained by integrating over the (-0.05 Å$^{-1} \leq q_z \leq 0.8$ Å^{-1}) region, and the peak was fitted using a Voight function (*solid line*). (*d*) Bragg rods corresponding to *b*. By integrating over the (1.3 Å$^{-1} \leq q_{xy} \leq 1.6$ Å^{-1}) region, the Bragg rod (*d*) was fitted (*solid line*) by approximating the coherently scattering part of the alkyl tail by a cylinder of constant electron density. In most cases, the resulting diffraction pattern after injection of cholera toxin was the combination of phase 1 (*a*) and phase 2 (*b*). The shoulder on the high q_{xy} side of the Bragg peak (indicated by arrow) in *c* is from the remaining monolayer phase where toxin did not bind.

(a 17% expansion from phase 1). In this configuration, the {1,−1} reflection at (q_{xy}, q_z) = (1.20 Å^{-1}, 1.05 Å^{-1}) is suppressed by the DW factor, and the FWHM of the Bragg peak (Fig. 8 *c*) gives a lateral coherence length (for the {0,1} and {1,0} peaks) of 232 Å.

More typical results of CTB_5 and $CTAB_5$ binding yield a mixture of phase 1 and phase 2

In most cases studied (listed below) the change in the observed diffraction patterns after injection of cholera toxin was more mild, and the Bragg rod data were modeled as a mixture of two phases. Phase 1 represented the structure of the bare monolayer (Fig. 8 *a*) or, in other words, where no toxin was bound. Phase 2 represented the highly tilted toxin-affected phase (Fig. 8 *b*). The use of two phases was supported by evidence that in most cases the toxin was not at full surface occupancy as seen by reflectivity results. Typical GIXD diffraction from the lipid tails with bound CTB_5 and $CTAB_5$ at pH = 8 is shown in Fig. 9 with structural parameters summarized in Table 1. In all cases, cholera toxin binding notably decreased the overall integrated intensity of the diffraction. Moreover, the ratio of intensity between the three resolved Bragg peaks was also altered, where peaks at lower q_{xy} had a larger intensity compared to the {1,−1} peak. Consequently, a two-phase system was required to model the intensity distribution along the Bragg rod after cholera toxin was bound.

The Bragg rod from the monolayer after $CTAB_5$ was bound is shown in Fig. 9 *b*. The figure is intended to illustrate the contribution of phase 1 and phase 2 to the total fit (phase 1 + phase 2). Similar diffraction patterns were obtained from monolayers with bound $CTAB_5$ + DTT, CTB_5, and CTB_5 + DTT (not shown). To model the Bragg rod, phase 1 was fixed to be identical to the bare monolayer while the height, tilt angle, tilt direction, and vertical DW factor of phase 2 were allowed to vary. In addition, a numerical factor was used to scale phase 1 relative to phase 2. The total fit (phase 1 + phase 2) was refined using a least-squares method. Over all data sets, the resulting amount of phase 2 ranged from 30% to 70%, consistent with the toxin coverage determined from reflectivity. Moreover, the fitted cylinder height of 18.6 ± 0.5 Å, tilt angle of 36.2 ± 2.0°, and DW factor of 2.6 ± 0.1 Å matched the modeled values from the extreme case (Fig. 8) when phase 2 was primarily present.

In-plane coherence lengths

Cholera binding and addition of DTT also had a large effect on the in-plane coherence lengths (L_{xy}) of the lipid tails (numerical values in Table 2). Before toxin was present, the L_{01}, L_{10}, and $L_{1\text{-}1}$ were 196 Å, 196 Å, and 670 Å, respectively. After cholera toxin was injected, the FWHM of the {0, 1} and {1, 0} Bragg peaks of phase 1 overlap with the Bragg peak of phase 2 and cannot be deconvolved. For this reason, only the $L_{1\text{-}1}$ lateral coherence length is presented after

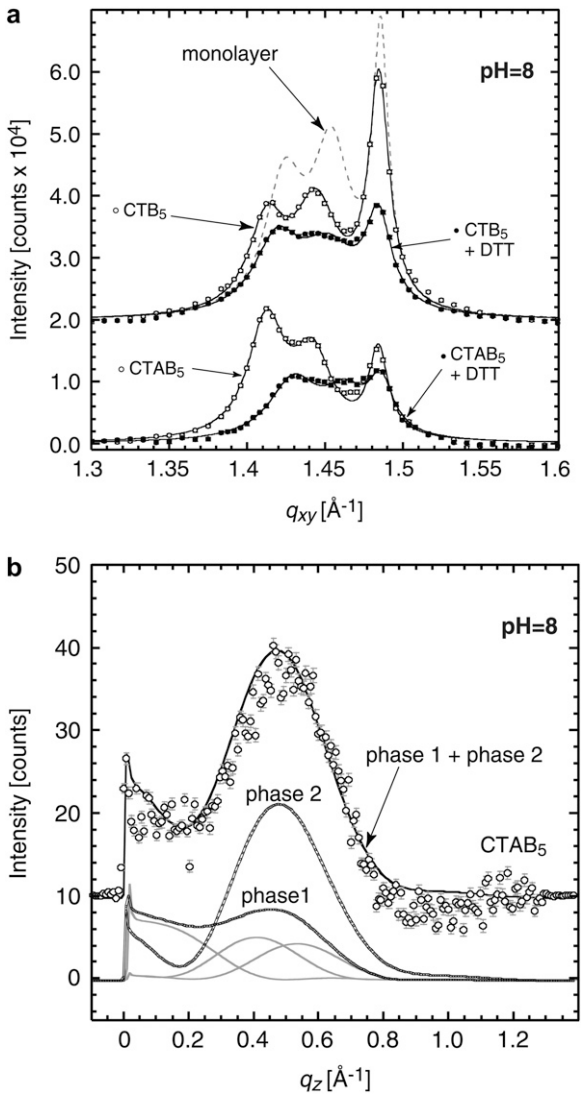

FIGURE 9 Bragg peaks and rods from GIXD measurements at pH = 8. (*a*) Bragg peaks for a DPPE:GM_1 monolayer with bound CTB_5, CTB_5 + DTT, $CTAB_5$, and $CTAB_5$ + DTT. Symbols represent measured data and lines represent the total (sum of three Bragg peaks) peak fit. Diffraction from the bare monolayer with no toxin present is shown as a dashed line for comparison. (*b*) The Bragg rod for a DPPE:GM_1 monolayer with bound $CTAB_5$ plotted with total fit (phase 1 + phase 2). Below, the contribution from phase 1 and phase 2 is shown. The lines under the phase 1 line are the individual {0,1}, {1,0} and {1,−1} Bragg rods for phase 1 similar to Fig. 7 *b*. For clarity, the CTB_5 and CTB_5 + DTT Bragg peaks in *a* have been offset vertically by 2×10^4 counts and the $CTAB_5$ Bragg rod in *b* by 10 counts. Molecular packing parameters used in the fits are listed in Table 1. Bragg rods, integrated over the $(q_{xy}, q_z) = (1.38-1.55\ \text{Å}^{-1}, -0.05-0.9\ \text{Å}^{-1})$ region, were fitted (*solid lines*) by using the sum of two phases. Phase 1 represented the structure of the bare monolayer (Fig. 8 *a*) or where no toxin was bound. Phase 2 represented the highly tilted toxin-affected phase (Fig. 8 *b*).

cholera toxin injection. After CTB_5 was bound, $L_{1\text{-}1}$ decreased from 670 Å to 415 Å. For CTB_5 + DTT, there was a 25% further reduction to $L_{1\text{-}1}$. This reduction is consistent with degradation of the monolayer order caused by toxin binding and/or toxin penetration. For $CTAB_5$ and $CTAB_5$ + DTT, there was similar decrease to the in-plane order compared to CTB_5 and CTB_5 + DTT. There were no significant changes in the diffraction pattern of the lipid tail peaks when DTT was added to the monolayer in the absence of toxin (data not shown), clearly demonstrating that toxin binding and addition of DTT were the cause of these monolayer perturbations. We hypothesize that the decreases in in-plane coherence lengths indicate perturbations to the lipid regions with bound toxin that could lead to initiation of endocytosis. Previous studies have demonstrated that membrane fusion becomes more likely when there is phase separation (33–36).

GIXD analysis (pH = 5)

Before and after injection of cholera toxin, there was only one significant difference between the diffraction from the monolayer when comparing between pH = 8 and pH = 5; both CTB_5 + DTT and $CTAB_5$ + DTT produced a larger decrease to the $L_{1\text{-}1}$ coherence length when compared to results at pH = 8. This result indicates that cholera toxin perturbs the lipid monolayer structure and phase more at low pH.

CONCLUSIONS

Using x-ray reflectivity, we were able to monitor the binding of cholera toxin, show that toxin surface coverage ranged between ~49% and 62%, and follow the penetration of the cholera toxin into the lipid monolayer at the air-water interface. In our earlier neutron reflectivity work, toxin penetration was inconclusive due to lower resolution (14). By modeling changes in the x-ray reflectivity data, a notable amount of toxin was observed to enter the lipid tail region in the case of $CTAB_5$ + DTT for both pH values. This suggests that $CTAB_5$ is capable of penetrating both the endosomal (pH5) and plasma (pH7) membrane. An increase in the electron density of the tail region was also observed for CTB_5 + DTT at pH = 8. This toxin penetration may indicate that the CTB_5 portion of the toxin, independent of the A subunit and before pH changes as a result of endocytosis, plays an active role in membrane penetration beyond binding the toxin to the membrane. Alternatively, we hypothesize that DTT may lead to conformational changes of the CTB_5 molecule at pH = 8 which aids penetration.

GIXD measurements provide precise information about the positional registry of the diffracting portion of the lipid monolayer and changes as a result of its interaction with toxin, while reflectivity measurements average over the entire sample in the beam footprint. As toxin was bound, the lateral ordering of lipids (2D cluster size) within the monolayer degraded, resulting in a decreased in-plane coherence length. The largest effect to the in-plane order was with $CTAB_5$ + DTT at pH = 5. This enhancement of toxin perturbation to the monolayer supports endocytosis (low pH) in the infection pathway, but significant toxin penetration was

TABLE 2 In-plane coherence lengths obtained from GIXD analysis

	In-plane Bragg peaks (pH = 8) Coherence length, L_{xy} (Å ± 5 Å)			In-plane Bragg peaks (pH = 5) Coherence length, L_{xy} (Å ± 5 Å)		
20 mN/m, 23°C	L_{01}	L_{10}	$L_{1\text{-}1}$	L_{01}	L_{10}	$L_{1\text{-}1}$
DPPE:GM_1	196	196	670	196	240	570
DPPE:GM_1 + CTB_5	*	*	415	*	*	415
DPPE:GM_1 + CTB_5 + DTT	*	*	311	*	*	278
DPPE:GM_1 + $CTAB_5$	*	*	455	*	*	455
DPPE:GM_1 + $CTAB_5$ + DTT	*	*	331	*	*	240

Length, L, is the in-plane coherence length; an average size of the 2-D ''crystalline'' islands.
*This value was not reported due to its convolution with the phase 2 Bragg peak.

also observed at high pH. These findings are consistent with biochemical studies that have established that cholera toxin signal transduction does not require acidification (37).

A new lipid phase was observed on binding cholera toxin. Previously, fluorescence measurements have shown that the binding of cholera toxin can cause uniform, single-phase membranes to phase-separate into large, coexistent liquid-ordered and liquid-disordered membrane domains (15). Diffraction from this toxin-affected phase (phase 2) revealed that the phase has a larger lipid tilt angle and area per headgroup despite a constant surface pressure of 20 mN/m. By confining five GM_1 lipid molecules to its B_5 pentamer, cholera toxin is able to disturb the lipid packing beneath it and create a new, more expanded lipid phase with a commensurate decrease in thickness of the lipid monolayer. Since our measurements were performed on a gel-phase monolayer at a constant surface pressure of 20 mN/m, it is possible that the amount of phase separation was restricted. Nevertheless, cholera toxin's ability to stimulate phase separation may invoke lateral stresses that could lead to endocytosis and uptake of the toxin into a cell or aid A1 subunit insertion into the membrane's hydrophobic interior as many partitioning proteins are intended to span a specific membrane thickness.

Though the study of a monolayer is only an approximation of a bilayer, these studies have enabled high-resolution characterization of cholera toxin binding and penetration into a lipid layer. Our studies using grazing incidence diffraction suggest that membrane perturbation caused by cholera toxin's binding unit, manifested as changes in the in-plane and out-of-plane order of the model lipid membrane, may be a mechanism for initiating endocytosis and uptake into the cell. Furthermore, increased perturbation of the monolayer caused by activated $CTAB_5$ at low pH supports the important role of low endosomal pH in the infection pathway. Our findings using x-ray reflectivity are sensitive enough to measure minute changes in electron density, occupancy, and disturbance of lipid order. Our findings further suggest that the B_5 pentamer may play a more active role in the membrane penetration mechanism than solely binding cholera toxin to its cell surface receptor.

We recognize Carlsberg, DanSync, HASYLAB for beamtime and for the courage to judge the safety issues on their merits and allow these experiments to be performed. We thank Dr. Kristian Kjaer for help with the reflectivity and grazing incidence diffraction experiments.

The Los Alamos Neutron Science Center at the Los Alamos National Laboratory (LANL) is funded by the U.S. Department of Energy (DOE) under Contract W-7405-ENG-36. J.M and C.E.M. thank the LANL–Laboratory Directed Research and Development program, DOE Office of Science (Basic Energy Sciences) for financial support. C.E.M. acknowledges support from the LANL Director's Post-Doctoral Fellowship and the Institute for Complex Adaptive Matter. T.L.K. thanks the Jeff and Dianne Child/Steve Whitaker Fund for Distinguished Teaching and Scholarship for financial support.

REFERENCES

1. Middlebrook, J. L., and R. B. Dorland. 1984. Bacterial toxins—cellular mechanisms of action. *Microbiol. Rev.* 48:199–221.
2. Zhang, R. G., D. L. Scott, M. L. Westbrook, S. Nance, B. D. Spangler, G. G. Shipley, and E. M. Westbrook. 1995. The three-dimensional crystal structure of cholera toxin. *J. Mol. Biol.* 251:563–573.
3. Zhang, R. G., M. L. Westbrook, E. M. Westbrook, D. L. Scott, Z. Otwinowski, P. R. Maulik, R. A. Reed, and G. G. Shipley. 1995. The 2.4 angstrom crystal structure of cholera toxin B subunit pentamer—choleragenoid. *J. Mol. Biol.* 251:550–562.
4. Feng, Y., A. P. Jadhav, C. Rodighiero, Y. Fujinaga, T. Kirchhausen, and W. I. Lencer. 2004. Retrograde transport of cholera toxin from the plasma membrane to the endoplasmic reticulum requires the trans-Golgi network but not the Golgi apparatus in Exo2-treated cells. *EMBO Rep.* 5:596–601.
5. Mekalanos, J. J., R. J. Collier, and W. R. Romig. 1979. Enzymic activity of cholera toxin. 2. Relationships to proteolytic processing, disulfide bond reduction, and subunit composition. *J. Biol. Chem.* 254:5855–5861.
6. Holmgren, J. 1981. Actions of cholera-toxin and the prevention and treatment of cholera. *Nature.* 292:413–417.
7. Venienbryan, C., P. F. Lenne, C. Zakri, A. Renault, A. Brisson, J. F. Legrand, and B. Berge. 1998. Characterization of the growth of 2d protein crystals on a lipid monolayer by ellipsometry and rigidity measurements coupled to electron microscopy. *Biophys. J.* 74:2649–2657.
8. Lauer, S., B. Goldstein, R. L. Nolan, and J. P. Nolan. 2002. Analysis of cholera toxin-ganglioside interactions by flow cytometry. *Biochemistry.* 41:1742–1751.
9. Ribi, H. O., D. S. Ludwig, K. L. Mercer, G. K. Schoolnik, and R. D. Kornberg. 1988. 3-Dimensional structure of cholera-toxin penetrating a lipid-membrane. *Science.* 239:1272–1276.
10. Yuan, C. B., and L. J. Johnston. 2000. Distribution of ganglioside GM1 in L-α-dipalmitoylphosphatidylcholine/cholesterol monolayers: a model for lipid rafts. *Biophys. J.* 79:2768–2781.
11. Yuan, C. B., and L. J. Johnston. 2001. Atomic force microscopy studies of ganglioside GM_1 domains in phosphatidylcholine and phosphatidylcholine/cholesterol bilayers. *Biophys. J.* 81:1059–1069.

12. Forstner, M. B., C. K. Yee, A. N. Parikh, and J. T. Groves. 2006. Lipid lateral mobility and membrane phase structure modulation by protein binding. *J. Am. Chem. Soc.* 128:15221–15227.

13. Terrettaz, S., T. Stora, C. Duschl, and H. Vogel. 1993. Protein-binding to supported lipid-membranes - investigation of the cholera-toxin ganglioside interaction by simultaneous impedance spectroscopy and surface-plasmon resonance. *Langmuir*. 9:1361–1369.

14. Miller, C. E., J. Majewski, R. Faller, S. Satija, and T. L. Kuhl. 2004. Cholera toxin assault on lipid monolayers containing ganglioside GM_1. *Biophys. J.* 86:3700–3708.

15. Hammond, A. T., F. A. Heberle, T. Baumgart, D. Holowka, B. Baird, and G. W. Feigenson. 2005. Crosslinking a lipid raft component triggers liquid ordered-liquid disordered phase separation in model plasma membranes. *Proc. Natl. Acad. Sci. USA*. 102:6320–6325.

16. Safran, S. A., T. L. Kuhl, and J. N. Israelachvili. 2001. Polymer-induced membrane contraction, phase separation, and fusion via Marangoni flow. *Biophys. J.* 81:659–666.

17. Rodighiero, C., Y. Fujinaga, T. R. Hirst, and W. I. Lencer. 2001. A cholera toxin B-subunit variant that binds ganglioside GM_1 but fails to induce toxicity. *J. Biol. Chem.* 276:36939–36945.

18. Hazes, B., and R. J. Read. 1997. Accumulating evidence suggests that several AB-toxins subvert the endoplasmic reticulum-associated protein degradation pathway to enter target cells. *Biochemistry*. 36:11051–11054.

19. Lencer, W. I., T. R. Hirst, and R. K. Holmes. 1999. Membrane traffic and the cellular uptake of cholera toxin. *Biochim. Biophys. Acta*. 1450: 177–190.

20. Majewski, J., T. L. Kuhl, K. Kjær, and G. S. Smith. 2001. Packing of ganglioside-phospholipid monolayers: an x-ray diffraction and reflectivity study. *Biophys. J.* 81:2707–2715.

21. Als-Nielsen, J., D. Jacquemain, K. Kjaer, F. Leveiller, M. Lahav, and L. Leiserowitz. 1994. Principles and applications of grazing incidence x-ray and neutron scattering from ordered molecular monolayers at the air-water interface. *Phys. Rep.* 246:252–313 [review].

22. Alsnielsen, J., and K. Kjaer. 1989. X-ray reflectivity and diffraction studies of liquid surfaces and surfactant monolayers. *In* T. Riste and D. Sherrington, editors. Plenum Press, Geilo, Norway. 113–137.

23. Jensen, T. R., and K. Kjaer. 2001. Novel methods to study interfacial layers: Structural properties and interactions of thin films at the air-liquid interface explored by synchrotron X-ray scattering. *In* Studies in Interface Science. D. Möbius and R. Miller, editors. Elsevier, Amsterdam. 205–254.

24. Kjaer, K. 1994. Some simple ideas on x-ray reflection and grazing-incidence diffraction from thin surfactant films. *Physica B*. 198:100–109.

25. Pedersen, J. S., and I. W. Hamley. 1994. Analysis of neutron and x-ray reflectivity data by constrained least-squares methods. *Physica B (Amsterdam).* 198:16–23.

26. Reference deleted in proof.

27. Gopal, A., and K. Y. C. Lee. 2006. Headgroup percolation and collapse of condensed Langmuir monolayers. *J. Phys. Chem. B*. 110:22079–22087.

28. Faller, R., and T. L. Kuhl. 2003. Modeling the binding of cholera toxin to a lipid membrane by a non-additive two-dimensional hard-disk model. *Soft Materials*. 1:343–352.

29. Miller, C. E., J. Majewski, E. B. Watkins, M. Weygand, and T. L. Kuhl. 2007. Part II: diffraction from 2D cholera toxin crystals bound to their receptors in a lipid monolayer. *Biophys. J.* 95:641–647.

30. Guinier, A. 1963. X-ray diffraction in crystals, imperfect crystals, and amorphous bodies. *In* W. H. Freeman, San Francisco.

31. Kjaer, K., J. Alsnielsen, C. A. Helm, P. Tippmannkrayer, and H. Mohwald. 1989. Synchrotron x-ray diffraction and reflectrion studies of arachidic acid monolayers at the air-water interface. *J. Phys. Chem.* 93:3200–3206.

32. Kaganer, V. M., I. R. Peterson, R. M. Kenn, M. C. Shih, M. Durbin, and P. Dutta. 1995. Tilted phases of fatty-acid monolayers. *J. Chem. Phys.* 102:9412–9422.

33. Hui, S. W., L. T. Boni, T. P. Stewart, and T. Isac. 1983. Identification of phosphatidylserine and phosphatidylcholine in calcium-induced phase separated domains. *Biochemistry*. 22:3511–3516.

34. Leckband, D. E., C. A. Helm, and J. Israelachvili. 1993. Role of calcium in the adhesion and fusion of bilayers. *Biochemistry*. 32:1127–1140.

35. Leventis, R., J. Gagne, N. Fuller, R. P. Rand, and J. R. Silvius. 1986. Divalent-cation induced fusion and lipid lateral segregation in phosphatidylcholine phosphatidic-acid vesicles. *Biochemistry*. 25:6978–6987.

36. Silvius, J. R., and J. Gagne. 1984. Lipid phase-behavior and calcium-induced fusion of phosphatidylethanolamine-phosphatidylserine vesicles—calorimetric and fusion studies. *Biochemistry*. 23: 3232–3240.

37. Lencer, W. I., G. Strohmeier, S. Moe, S. L. Carlson, C. T. Constable, and J. L. Madara. 1995. Signal-transduction by cholera-toxin—processing in vesicular compartments does not require acidification. *Am. J. Physiol. Gastr. L.* 32:G548–G557.

38. Vineyard, G. H. 1982. Grazing-incidence diffraction and the distorted-wave approximation for the study of surfaces. *Phys. Rev. B*. 26:4146–4159.